Optics Letters

Automated computational aberration correction method for broadband interferometric imaging techniques

Paritosh Pande,[1,†] Yuan-Zhi Liu,[1,2,†] Fredrick A. South,[1,2] and Stephen A. Boppart[1,2,3,4,*]

[1]*Beckman Institute for Advanced Science and Technology, University of Illinois at Urbana-Champaign, Urbana, Illinois 61801, USA*
[2]*Department of Electrical and Computer Engineering, University of Illinois at Urbana-Champaign, Urbana, Illinois 61801, USA*
[3]*Department of Bioengineering, University of Illinois at Urbana-Champaign, Urbana, Illinois 61801, USA*
[4]*Department of Medicine, University of Illinois at Urbana-Champaign, Urbana, Illinois 61801, USA*
Corresponding author: boppart@illinois.edu

Numerical correction of optical aberrations provides an inexpensive and simpler alternative to the traditionally used hardware-based adaptive optics techniques. In this Letter, we present an automated computational aberration correction method for broadband interferometric imaging techniques. In the proposed method, the process of aberration correction is modeled as a filtering operation on the aberrant image using a phase filter in the Fourier domain. The phase filter is expressed as a linear combination of Zernike polynomials with unknown coefficients, which are estimated through an iterative optimization scheme based on maximizing an image sharpness metric. The method is validated on both simulated data and experimental data obtained from a tissue phantom, an *ex vivo* tissue sample, and an *in vivo* photoreceptor layer of the human retina. © 2016 Optical Society of America

OCIS codes: (110.4500) Optical coherence tomography; (110.3175) Interferometric imaging; (110.1758) Computational imaging; (110.1080) Active or adaptive optics.

Aberrations in an optical system cause a reduction in imaging resolution and poor image contrast, and limit the imaging depth while imaging biological samples. Traditional hardware-based adaptive optics (HAO) methods provide a means for correcting these aberrations by physically sensing and modifying the wavefront by using a wavefront sensor and deformable mirror, respectively [1]. HAO methods have complex optical setups and require expensive components. In interferometry-based imaging techniques such as digital holography microscopy (DHM) and optical coherence tomography (OCT)/optical coherence microscopy (OCM), the measurement of a complex optical field allows for computational correction of aberrations by numerically modifying the phase of the detected signal. Compared to HAO-based methods, computational aberration correction offers the flexibility of correcting the aberrations post-data-acquisition without the need for expensive and complex hardware used in HAO.

A group of computational aberration correction techniques is based on numerical sensing of the aberrated wavefront. In the context of OCT/OCM imaging, the guide star-based numerical correction method proposed by Adie *et al.* [2] and the subaperture correlation-based wavefront error sensing and correction method proposed by Kumar *et al.* [3] belong to this category. The guide star method is particularly well-suited for images that contain point-like structures. However, because not all samples contain natural guide stars, the applicability of this method can be limiting. The numerical subaperture correlation technique is more general than the guide star method, but the requirement of a uniform Fourier spectrum, and the trade-off between cross-correlation accuracy (subaperture size) and wavefront precision (subaperture number) makes the performance of this method dependent on the scattering properties of samples. Another group of techniques for computational aberration correction is based on estimating an optimal complex pupil phase profile for aberration correction.

Previously, our group has successfully demonstrated a numerical aberration correction technique called computational adaptive optics (CAO) for OCT imaging of various tissue phantoms and samples [4–6]. The CAO technique is based on maximizing an image sharpness metric to optimize the pupil phase profile, which is modeled as a linear combination of Zernike polynomials. In the existing implementation of our CAO technique, the optimization of the pupil function is performed by manually changing the coefficients of the Zernike polynomials while monitoring the trend of the sharpness metric. In this Letter, we present an automated approach for performing CAO, wherein the optimal Zernike polynomial coefficients are obtained through an iterative optimization method.

The idea of correcting aberrations by maximizing a sharpness metric has been, in the past, proposed and used for both incoherent and coherent imaging systems [7,8]. In the HAO-based OCT literature, the idea is used in sensorless AO systems, where, most commonly, the coefficients of a subset of Zernike basis functions are sequentially optimized in a predetermined

order using a 1D grid search algorithm to alter the shape of the deformable mirror so as to achieve maximum image sharpness [9–11]. While this simple approach is fast and requires only a few measurements, which is advantageous for *in vivo* imaging, it does not necessarily guarantee an optimal solution. This is because an optimum solution in one dimension of a multidimensional space does not necessarily correspond to the optimum value of the same dimension in the original multidimensional space. Moreover, the choice of the order in which the different Zernike modes are optimized seems unclear [9,10,12,13]. To circumvent these problems, in our optimization routine, instead of optimizing a predetermined Zernike mode at a time, the number and type of Zernike modes at each optimization step are chosen randomly. Starting from an initial point, for different runs of the algorithm, the subsequent random selection of the Zernike modes in our approach allows for the exploration of different trajectories possibly leading to different optima in the multivariate search space. Additionally, instead of using a 1D grid search algorithm for optimization, we use the **R**esilient back**prop**agation (Rprop) algorithm, which was originally proposed as an alternative to the gradient-descent based backpropagation algorithm for training the weights in a multilayer feedforward neural network [14].

To understand the optimization problem we seek to solve, consider a complex valued aberrant image $g(x, y)$ and the corresponding Fourier-domain representation $G(u, v)$. In OCT/OCM, $g(x, y)$ can be an *en face* complex image extracted from the three-dimensional (3D) data after standard OCT processing. The process of correcting aberrations can be viewed as introducing a suitable phase correction term to $\phi(u, v)$ to the aberrant image in the Fourier domain to obtain the corrected image, as follows:

$$H(u, v) = G(u, v)e^{-j\phi(u,v)}, \tag{1}$$

such that sharpness of the corrected image, defined as

$$S = \sum_{x,y}[h(x, y)h^*(x, y)]^2, \tag{2}$$

is maximized, where $h(x, y)$ is related to $H(u, v)$ by a Fourier transform, i.e., $H(u, v) = \mathcal{F}[h(x, y)]$. Expressing the phase correction term as a weighted sum of Zernike polynomials, $\psi_k(u, v)$,

$$\phi(u, v) = \sum_{k=1}^{K} c_k \psi_k(u, v), \tag{3}$$

the problem of obtaining the corrected image $h(x, y)$ is then equivalent to finding the optimal weights or coefficients, $\hat{\mathbf{c}} = [\hat{c}_1, \hat{c}_2, ..., \hat{c}_K]^T$ for the Zernike modes that maximize the image sharpness defined as in Eq. (2). Algorithm 1 outlines the main steps of the procedure used to optimize the Zernike mode coefficients. At each iteration of the algorithm, a random number of Zernike modes are selected (step 4 in Algorithm 1). The coefficients for the selected Zernike modes are then optimized by using the Rprop algorithm (step 5). After obtaining the optimized coefficients, $\tilde{c}^{\text{opt}}$, all the Zernike polynomial coefficients are updated (step 11) to reflect the cumulative correction applied to the original aberrant image. Finally, the phase correction is applied to the aberrant image to obtain a corrected image, which serves as the aberrant image in the next iteration (step 12). Moreover, to explore multiple optima, the optimization procedure was run five times and the solution yielding the largest value of the sharpness metric was accepted as the final solution.

Algorithm 1 Optimization of Zernike Coefficients

Input: $\text{I}^{\text{abb}} \equiv g(x, y) \in \mathbb{R}^{\text{M}\times\text{N}}$, $\text{ZP} \in \mathbb{R}^{\text{M}\times\text{N}\times\text{K}}$
Output: $\text{I}^{\text{corr}} \equiv h(x, y) \in \mathbb{R}^{\text{M}\times\text{N}}$, $\text{c}^{\text{opt}} \equiv \hat{\mathbf{c}} \in \mathbb{R}^{\text{K}\times 1}$
1:   $\text{I}^{\text{corr}} \leftarrow \text{I}^{\text{abb}}$
2:   $\text{c}^{\text{opt}} \leftarrow \text{zeros}(\text{K}, 1)$
3:   **repeat**
4:     $k \equiv \text{logical}[X_1, X_2, ..., X_K]: X_k \sim \text{Bernoulli}(0.5)$
      $\forall \, k \in \{1, 2, ..., K\}$ such that not all $X_k \in \{0, 1\}$
5:     $\tilde{c}^{\text{opt}} \leftarrow \text{Rprop}(\text{I}^{\text{corr}}, \text{ZP}(:, :, k))$
6:     $\phi \leftarrow \text{zeros}(M, N)$
7:     $k_{\text{nonzero}} \leftarrow \text{find}(k)$
8:     **for** $k_{\text{index}} = 1{:}\text{length}(\tilde{c}^{\text{opt}})$ **do**
9:       $\phi \leftarrow \phi + \tilde{c}^{\text{opt}}(k_{\text{index}}) * \text{ZP}(:, :, k_{\text{nonzero}}(k_{\text{index}}))$
10:    **end for**
11:    $\text{c}^{\text{opt}}(k_{\text{nonzero}}) \leftarrow \text{c}^{\text{opt}}(k_{\text{nonzero}}) + \tilde{c}^{\text{opt}}$
12:    $\text{I}^{\text{corr}} \leftarrow \mathcal{F}^{-1}\{\mathcal{F}\{\text{I}^{\text{corr}}\}. * \exp(-1i * \phi * \text{ZP})\}$
13:   **until** converged

The choice of the Rprop algorithm used as the optimization method in our study was primarily motivated by the simplicity of the algorithm and the robustness of its performance to the choice of the various parameters of the algorithm. Here, we briefly outline the basic steps of the algorithm in the context of our problem. More details regarding the implementation and comparison of the Rprop algorithm with other optimization methods can be found elsewhere [14–16]. The algorithm starts by setting the initial update values for all Zernike polynomial weights to Δ_0. This parameter determines the size of the first weight step and was set to 0.01 in this study. The choice of this parameter is rather uncritical because the weight steps are adaptively changed during the course of the optimization, as discussed next. The subsequent update value for each weight is adaptively determined based on the change in the sign of the partial derivative of the sharpness metric with respect to the corresponding weight. Every time the partial derivative of a weight $\nabla_{c_k} S^{(t)}$ changes sign, which indicates that the last update for that weight was too large, and causing the algorithm to jump over a maximum point, the update value $\Delta_k^{(t)}$ is decreased by a factor of η^-. If, however, the sign of the derivative is unchanged, then the update value is incremented by a factor of η^+ to accelerate the convergence process. Based on the recommendations of the developers of Rprop, η^+ and η^- were set to 0.5 and 1.2, respectively. To avoid the weights from becoming too large or too small, the update values are bounded by an empirically determined upper limit $\Delta_{\max}$ and a lower limit $\Delta_{\min}$:

$$\Delta_k^{(t)} = \begin{cases} \max(\eta^+ * \Delta_k^{(t-1)}, \Delta_{\max}) & \text{if } \nabla_{c_k} S^{(t-1)} * \nabla_{c_k} S^{(t)} > 0 \\ \min(\eta^- * \Delta_k^{(t-1)}, \Delta_{\min}) & \text{if } \nabla_{c_k} S^{(t-1)} * \nabla_{c_k} S^{(t)} < 0 \\ \Delta_k^{(t-1)} & \text{otherwise.} \end{cases} \tag{4}$$

The coefficient update value thus obtained can then be used to obtain the new coefficient value based on the sign of the derivative as follows:

$$c_k^{(t+1)} = \begin{cases} c_k^{(t)} + \Delta_k^{(t)} & \text{if } \nabla_{c_k} S^{(t)} > 0 \\ c_k^{(t)} - \Delta_k^{(t)} & \text{if } \nabla_{c_k} S^{(t)} < 0 \\ c_k^{(t)} & \text{otherwise.} \end{cases} \tag{5}$$

Finally, following the derivation in [17] an expression for the partial derivative of the sharpness metric can be analytically obtained as

$$\nabla_{c_k} S = \sum_{x,y} |h_i(x,y)|^2 \Im \left\{ \sum_{u,v} H_i(u,v) \omega_M^{ux} \omega_N^{vy} \psi_k(u,v) h_i^*(x,y) \right\},$$

(6)

where the subscript i denotes the intermediate value for each iteration step, M, and N denotes the number of pixels in the image along the lateral dimensions, $\omega_M = e^{2\pi j/M}$ denotes a primitive Mth root of unity, and $\Im\{z\}$ denotes the imaginary part of z.

The performance of the proposed algorithm was first validated on a simulated U.S. Air Force (USAF) resolution test target image. A mixture of Gaussian and speckle noise was added to the original image to simulate a noisy image. Next, optical aberrations were introduced to the simulated noisy image by adding a phase term to the nonaberrant image in Fourier domain. Similar to previous works on sensorless AO [9,12,13], the phase term was modeled as a weighted sum of Zernike polynomials corresponding to the following six primary aberrations: defocus, astigmatism (0°), astigmatism (45°), coma (0°), coma (45°), and spherical aberration. To mimic a general optical aberration, the weights of the Zernike polynomials were randomly chosen. The aberrant noisy image thus generated is shown in Fig. 1(a), which was used as the input to our aberration correction algorithm. The image obtained after aberration correction is shown in Fig. 1(b), which, when compared to the aberrant image, has significantly better contrast and reduced aberrations.

After validating the performance of the proposed aberration correction algorithm on a simulated image, the algorithm was tested for OCT/OCM images of various samples. Figure 2(a) shows an aberrant *en face* OCM image of a tissue mimicking phantom consisting of copper zinc iron oxide nanoparticles (<100 nm) in PDMS. The *en face* image corresponds to a plane located 30.4 µm above the focus and extracted from the 3D volumetric data set, which was acquired using a high NA (NA = 0.6) Fourier-domain OCM system described elsewhere [5]. The image shows significant blurring resulting from the broadening of the point spread function (PSF) due to the presence of the aberrations. A zoomed-in view of the area enclosed by the blue dashed rectangle in Fig. 2(a) shows the severity of the aberrations. After aberration correction, as expected, the image SNR is improved and the subresolution nanoparticles appear as point-like structures, as shown in
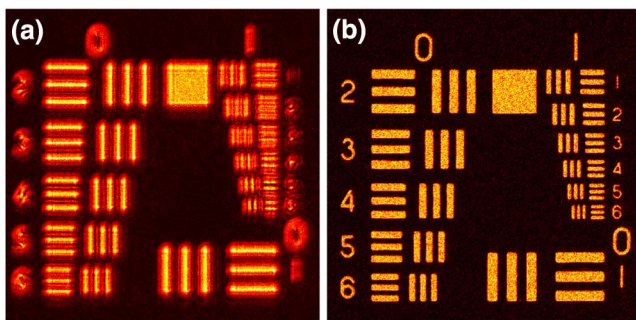
Fig. 1. (a) Simulated USAF resolution test target image with introduced aberrations. (b) Recovered image after automated aberration correction.
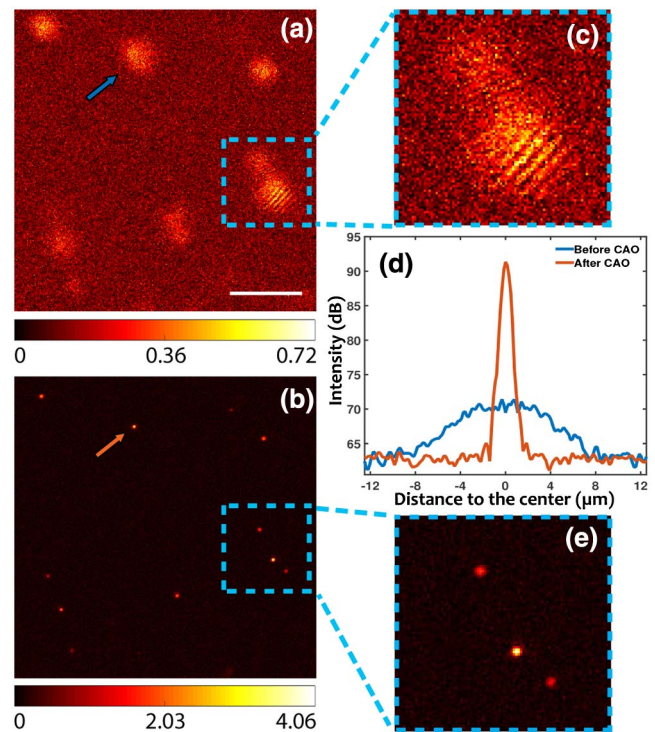

Fig. 2. *En face* OCM images of sub-resolution particles in a tissue mimicking phantom before (a) and after (b) CAO correction. (c) and (e) are zoomed-in images of the regions enclosed by the blue dashed squares in (a) and (b), respectively. The color bar scales indicate significant improvement of the peak intensity of the signal after aberration correction. (d) PSF measurements for the particles indicated by arrows in (a) and (b). The scale bar denotes 25 µm.

Fig. 2(b) and the corresponding zoomed-in view in Fig. 2(e). A comparison of the zoomed-in views shows that the three particles, which are indistinguishable in Fig. 2(c) due to the presence of aberrations, can be clearly resolved in Fig. 2(e). Additionally, as shown in Fig. 2(d), the PSF obtained after aberration correction (orange curve) is significantly narrower than the PSF obtained from the aberrant image (blue curve). Specifically, after CAO processing, the full-width-at-half-maximum (FWHM) of the PSF was estimated to be 0.8 µm, which was the diffraction limit of the OCM system.

Next, the algorithm was tested on an OCM image acquired from a scattering biological sample, which in our case was *ex vivo* adipose tissue surrounding the aorta from an atherosclerotic rabbit. The OCM system used for imaging was the same as was used for the tissue mimicking phantom. The aberrant *en face* OCM image corresponding to a plane at 37 µm above the focal plane and the corrected image are shown in Figs. 3(a) and 3(b), respectively. The corrected image clearly has better contrast than the aberrant image, and the membrane boundaries of the adipose tissue are also much better delineated in the corrected image.

Finally, the proposed aberration correction algorithm was used and tested on an *en face* OCT image acquired *in vivo* from the retinal photoreceptor layer in a human subject. The parafoveal cone image was acquired using a high-speed *en face* OCT system, details of which have been reported in an earlier publication [6]. Unlike the adipose tissue, the photoreceptor layer is a
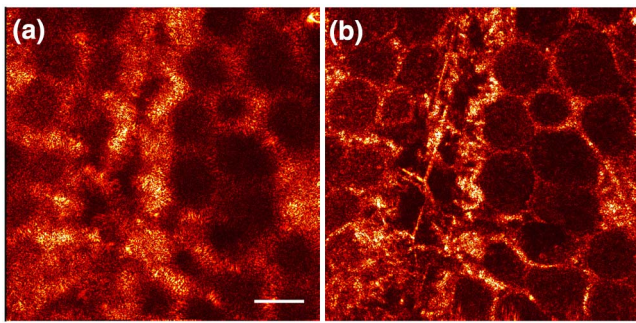
Fig. 3. *En face* images from rabbit adipose tissue: (a) before CAO correction and (b) after CAO correction. The scale bar denotes 50 μm.

strongly backscattering sample. Due to optical aberrations, the individual cones are not recognizable in the raw *en face* OCT image as shown in Fig. 4(a). After CAO correction, the cones become clearly visible and well resolved throughout the entire image as shown in Fig. 4(b). The enhancement in image resolution is also supported by the improved intensity of the peak in the plot of radially averaged power spectrum of the cone mosaic indicated by the black arrow in Fig. 4(c), which corresponds to the radius of Yellott's ring and is an indicator of the improved periodicity of the regularly arranged photoreceptors. Figure 4(c) also shows that the amplitude of higher spatial frequency components has been improved, which suggests finer structures over the entire field-of-view in the corrected image are better resolved than in the raw image before applying CAO.
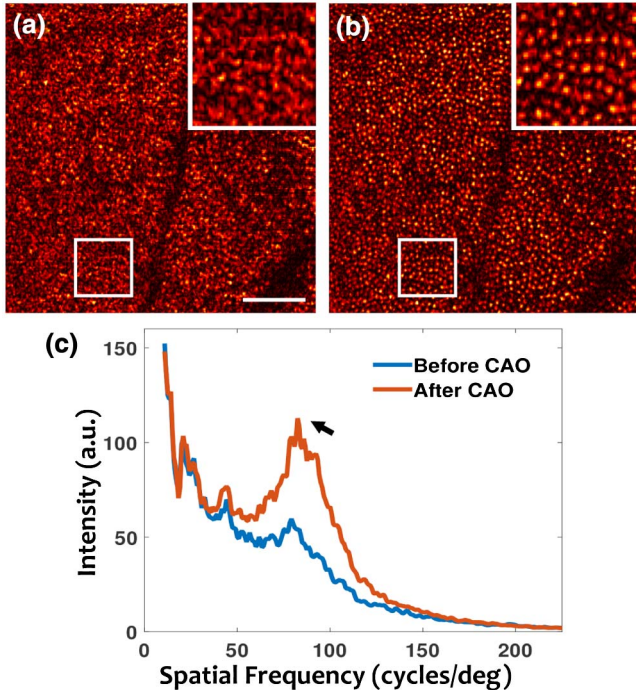
Fig. 4. Imaging of the living human photoreceptors in the parafoveal region. (a) *En face* OCT of the cone mosaic before aberration correction. (b) Cone mosaic after automated aberration correction. The insets show zoomed-in views of the regions in white squares. (c) Radially averaged power spectrum of (a) and (b). The peak indicated by the black arrow corresponds to the radius of Yellott's ring. The scale bar represents 0.25°.

In summary, we have proposed and demonstrated an automated method for computational aberration correction in broadband interferometry techniques. The ability of the proposed method to successfully correct aberrations was demonstrated with OCT/OCM images of simulated, *ex vivo*, and *in vivo* samples, having different scattering properties. The number of iterations, the change in sharpness metric, and the computational time of the proposed algorithm depend on a multitude of factors, such as the nature of the structures present in the image, the amount of aberrations, the number of Zernike modes that are sought to be optimized, and the size of the image, in addition to the stochasticity of our approach. In its current implementation, the average time required for correcting six primary aberrations in the USAF target image (image size: 512×512) on a Windows machine with an Intel i7 3.3 GHz processor and 16 GB RAM was 20 s. Although the processing time is not extremely crucial for our applications because CAO processing is performed post-data-acquisition, it might nevertheless be advantageous, especially for clinical applications, where rapid aberration correction might be a requirement during imaging. In this regard, a graphic-processing-unit (GPU) based implementation of the proposed method might be worth exploring and will be pursued in future work.

REFERENCES

1. M. J. Booth, Philos. Trans. R. Soc. London Ser. A **365**, 2829 (2007).
2. S. G. Adie, N. D. Shemonski, B. W. Graf, A. Ahmad, P. S. Carney, and S. A. Boppart, Appl. Phys. Lett. **101**, 221117 (2012).
3. A. Kumar, W. Drexler, and R. A. Leitgeb, Opt. Express **21**, 10850 (2013).
4. S. G. Adie, B. W. Graf, A. Ahmad, P. S. Carney, and S. A. Boppart, Proc. Natl. Acad. Sci. USA **109**, 7175 (2012).
5. Y.-Z. Liu, N. D. Shemonski, S. G. Adie, A. Ahmad, A. J. Bower, P. S. Carney, and S. A. Boppart, Biomed. Opt. Express **5**, 2988 (2014).
6. N. D. Shemonski, F. A. South, Y.-Z. Liu, S. G. Adie, P. S. Carney, and S. A. Boppart, Nat. Photonics **9**, 440 (2015).
7. R. A. Muller and A. Buffington, J. Opt. Soc. Am. **64**, 1200 (1974).
8. R. G. Paxman and J. Marron, in *32nd Annual Technical Symposium* (International Society for Optics and Photonics, 1988), pp. 37–47.
9. S. Bonora and R. Zawadzki, Opt. Lett. **38**, 4801 (2013).
10. Y. Jian, J. Xu, M. A. Gradowski, S. Bonora, R. J. Zawadzki, and M. V. Sarunic, Biomed. Opt. Express **5**, 547 (2014).
11. Y. Xu, Y.-Z. Liu, S. A. Boppart, and P. S. Carney, Appl. Opt. **55**, 2034 (2016).
12. E. Grisan, F. Frassetto, V. Da Deppo, G. Naletto, and A. Ruggeri, Appl. Opt. **46**, 6434 (2007).
13. A. Jewel, V. Akondi, and B. Vohnsen, J. Eur. Opt. Soc. **8**, 13073 (2013).
14. M. Riedmiller and H. Braun, in *IEEE International Conference on Neural Networks* (IEEE, 1993), pp. 586–591.
15. M. Riedmiller, Comput. Stand. Interfaces **16**, 265 (1994).
16. M. Riedmiller, "Rprop-Description and Implementation Details," Technical Report (Inst. f. Logik, Komplexität u. Deduktionssysteme, 1994).
17. J. Fienup and J. Miller, J. Opt. Soc. Am. A **20**, 609 (2003).